

The devil is in the tails: the role of globular cluster mass evolution on stream properties

Eduardo Balbinot^{*} and Mark Gieles

Department of Physics, University of Surrey, Guildford GU2 7XH, UK

17 February 2022

ABSTRACT

We present a study of the effects of collisional dynamics on the formation and detectability of cold tidal streams. A semi-analytical model for the evolution of the stellar mass function was implemented and coupled to a fast stellar stream simulation code, as well as the synthetic cluster evolution code EMACSS for the mass evolution as a function of a globular cluster orbit. We find that the increase in the average mass of the escaping stars for clusters close to dissolution has a major effect on the observable stream surface density. As an example, we show that Palomar 5 would have undetectable streams (in an SDSS-like survey) if it was currently three times more massive, despite the fact that a more massive cluster loses stars at a higher rate. This bias due to the preferential escape of low-mass stars is an alternative explanation for the absence of tails near massive clusters, than a dark matter halo associated with the cluster. We explore the orbits of a large sample of Milky Way globular clusters and derive their initial masses and remaining mass fraction. Using properties of known tidal tails we explore regions of parameter space that favour the detectability of a stream. A list of high probability candidates is discussed.

Key words: globular clusters: general, Galaxy: structure

1 INTRODUCTION

Stellar streams are the long promised probes of the gravitational potential in galaxies. In the Milky Way (MW) these streams are visible as resolved stellar populations and upon the advent of large photometric surveys such as the Sloan Digital Sky Survey (SDSS; Ahn et al. 2014) and the Dark Energy Survey (DES; The Dark Energy Survey Collaboration 2005) began to be discovered in large numbers. These surveys revealed two types of streams: hot streams from disrupted high velocity dispersion, dark matter dominated dwarf galaxies, and cold streams from existing or completely dissolved globular clusters (GCs). The most remarkable examples of each type are the Sagittarius stream, a hot stream covering most of the sky (Newberg et al. 2002) and the tidal tails of Palomar 5, a 22° long cold stellar stream (Odenkirchen et al. 2001; Grillmair & Dionatos 2006; Bernard et al. 2016).

While both kinds of streams are promising proxies of the gravitational potential of the MW (e.g. Koposov et al. 2010; Gibbons et al. 2014), cold streams are appealing because of their simplicity and long phase mixing time (Helmi & White 1999). The progenitors of cold streams are GCs which have internal velocity dispersion ($\lesssim 10 \text{ km s}^{-1}$), much lower than their orbital velocity (a few 100 km s^{-1}). Stars that become unbound follow approximately the same orbit (with some offset, as shown by Eyre & Binney 2009).

Each unbound star can be seen as a test particle for the MW gravitational potential while the collection of escaper stars should approximately trace a single orbit in the underlying potential (Koposov et al. 2010).

Several studies fail to find convincing signs of tails around MW GCs (Leon et al. 2000; Kuzma et al. 2016). The absence of tails may point at the presence of a dark matter halo surrounding the GC, preventing the stars from escaping (Moore 1996). The lack of tails associated with a GC could also be because the GC is in a weak tidal field. This may explain the absence of tails from GCs at large Galactic centre, but not why there are no cold streams associated with massive GCs. From theory and numerical results we know that the mass-loss rate as the result of evaporation depends on the cluster mass M and the Galactocentric distance R_G as: $\dot{M} \propto -M^{1/4}/R_G$, for clusters evolving in an isothermal halo (Baumgardt 2001; Gieles, Heggie & Zhao 2011). However, the most prominent cold streams observed are either progenitor-less or from low-mass GCs. One possible observational bias, proposed by Leon et al. (2000), is the preferential loss of low-mass stars, which makes streams fainter. Indeed, observations show many GCs have mass functions that are depleted in low-mass stars (see e.g. Paust et al. 2010).

In this paper we further investigate the interplay between the internal dynamics of GCs and its effect on the formation and structure of tidal tails. We focus on the preferential loss of low-mass stars due to mass segregation in the cluster and the evolution of

^{*} e.balbinot@surrey.ac.uk

2 Balbinot & Gieles

the velocity dispersion of potential escaper stars, i.e. stars that are energetically unbound, but still association with the cluster (see [Fukushige & Heggie 2000](#)).

This paper is organized as follows: in section 2 we describe a method to evolve a GC mass function as it loses mass while orbiting the Galaxy. In section 3 we present a simple model for the mass evolution of a cluster in the Galaxy as well as up-to-date orbital parameters and mass estimates for a large sample of MW GCs. In section 4 we explore the conditions for the observability of cold streams and highlight noteworthy candidates for the search of streams. In section 5 we use a spray-particle tidal tail simulation of Palomar 5 to illustrate the impact of the preferential loss of low-mass stars in the visibility of tidal tails. In section 6 we give our conclusions in the light of upcoming surveys.

2 METHOD

Ideally, we would like to map progenitor properties (i.e. initial mass and orbit) to stream properties such as length, width, particle mass, and velocity dispersion. In the case of GCs this comes at the cost of N -body models which are computationally expensive. To avoid the complications of such models, we choose to use the fast cluster evolution code Evolve Me A Cluster of Stars¹ (EMACSS, [Alexander & Gieles 2012](#); [Gieles et al. 2014](#); [Alexander et al. 2014](#)) EMACSS evolves several global cluster properties, such as the total bound mass M and number of stars N , half-mass radius r_h , and parameters describing the degree of mass segregation and the profile of the cluster via coupled ordinary differential equations (ODEs). These ODEs include the effect of escape of stars over the tidal boundary (evaporation), mass-loss as the result of stellar evolution and the diffusion of energy as the result of two-body relaxation on M , N and r_h . After a number of relaxation times have elapsed, the cluster is assumed to reach a stage of balanced evolution, in which the rate of change of the total cluster energy E is set by the flow of energy through r_h , following [Hénon \(1961\)](#). For full details on the implementation we refer to [Alexander et al. \(2014\)](#). The code needs only a fraction of a second to evolve a cluster until dissolution and the computational effort is N -independent. The code considers the effects of mass loss and expansion of the cluster as the result of stellar evolution, two-body relaxation and escape of stars due to a (static) tidal field. On top of the existing EMACSS implementation, we build a semi-analytical prescription of the evolution of the mass function which is described in detail in the following section.

2.1 Mass function evolution

In this section we present an algorithm to numerically evolve the stellar mass function (MF). Various prescriptions for the time-dependent MF exist (e.g. [Kruijssen 2009](#); [Lamers et al. 2013](#)). We aim to develop a prescription that can be coupled to the fast cluster code EMACSS. Because EMACSS solves a set of coupled ODEs, we develop a prescription for the rate of change of the number of stars and stellar remnants as a function of stellar mass m . We aim to correctly describe the preferential ejection of low-mass stars as the result of two-body relaxation, and the formation of stellar remnants as the result of stellar evolution. Below we describe the algorithm.

To evolve the MF of stars and remnants, we define $n_{\text{bin}} \simeq 100$ logarithmically spaced mass bins between $0.1 M_\odot$ and $100 M_\odot$. At

$t = 0$ the number of stars in each bin, N_j , is found from the stellar initial mass function (IMF, dN/dm_i , where m_i is the initial mass of a star), the total number of stars in the cluster N and the width of the individual bins Δm_j as

$$N_j = N \left. \frac{dN}{dm_i} \right|_{m_j} \Delta m_j \quad (1)$$

such that $\sum_{j=1}^{n_{\text{bin}}} N_j = N$ and $\sum_{j=1}^{n_{\text{bin}}} N_j m_j = M_i$, where M_i is the initial mass of the cluster. We then consider that $N_j = N_j^s + N_j^r$, with N_j^s the number of stars and N_j^r the number of stellar remnants as a function of mass. At $t = 0$ there are no remnants.

We then solve for N_j^s and N_j^r by integrating expressions for the rate of change of $\dot{N}_j = \dot{N}_j^s + \dot{N}_j^r$. Both stellar evolution and escape of stars contribute to these rates, which we discuss in the next sections.

2.2 Stellar evolution

To evolve stars by stellar evolution, we move stars that reach the end their main sequence life from N_j^s to N_j^r . We approximate the main-sequence lifetimes by

$$\tau_{\text{ms}}(m_i) = 0.21 \exp(10.4 m_i^{-0.322}), \quad (2)$$

which describes the main sequence life times of stars $0.5 < m_i/M_\odot < 30 M_\odot$ and $[\text{Fe}/\text{H}] = -0.5$ to within 10% compared to the SSE (Single-Star Evolution) models of [Hurley et al. \(2000\)](#), which provides a set of analytic relations that approximate the evolution of stars of different masses and chemical composition. In our MF evolution method, stars are assumed to have a constant mass m_i until $\tau_{\text{ms}}(m_i)$ is reached and then their mass is reduced by a factor

$$f^{\text{ifm}} = \begin{cases} 0 & m_i > 10 M_\odot, \\ 0.56(m_i/M_\odot)^{-0.56} & m_i \leq 10 M_\odot. \end{cases} \quad (3)$$

Removing all stars with $m_i > 10 M_\odot$ corresponds to 0% retention of black holes. A single relation for the masses of neutron stars and white dwarfs reproduces the results from SSE to within 10%. The most massive neutron stars is $1.54 M_\odot$ and a solar mass star results in a $0.56 M_\odot$ white dwarf.

We introduce stellar evolution by removing stars at a rate

$$\dot{N}_j^{\text{sev}} = \begin{cases} -N_j^s \left(\frac{t - \tau_{\text{ms},r}}{\sigma_t} \right), & t > \tau_{\text{ms},r}, \\ 0, & t < \tau_{\text{ms},r}, \end{cases} \quad (4)$$

where $\tau_{\text{ms},r}$ is the main sequence life time of a star with $m_j + 0.5\Delta m_j$ (i.e. corresponding to the right side of bin j) and σ_t sets the speed with which the bin is emptied. From experiments we find smooth evolution of the mass function when using $\sigma_t = 0.7(\tau_{\text{ms},r} - \tau_{\text{ms},l})$, where $\tau_{\text{ms},l} = \tau_{\text{ms}}(m_j - 0.5\Delta m_j)$ i.e. the life time of a star with mass corresponding to the left side of bin j .

While stars are being removed, remnants are being created, hence we fill bins of the remnants mass function at a rate

$$\dot{N}_k^r(m_{\text{TO}}(t) f^{\text{ifm}}) = -\dot{N}_j^{\text{sev}}, \quad (5)$$

where $m_{\text{TO}}(t)$ is the turn-off mass at time t , which is found from the inverse of the main sequence time relation (equation 2). The minus sign ensures that $\dot{N}_k^r \geq 0$ (note that $\dot{N}_j^{\text{sev}} < 0$).

¹ Available from <https://github.com/emacss/emacss>

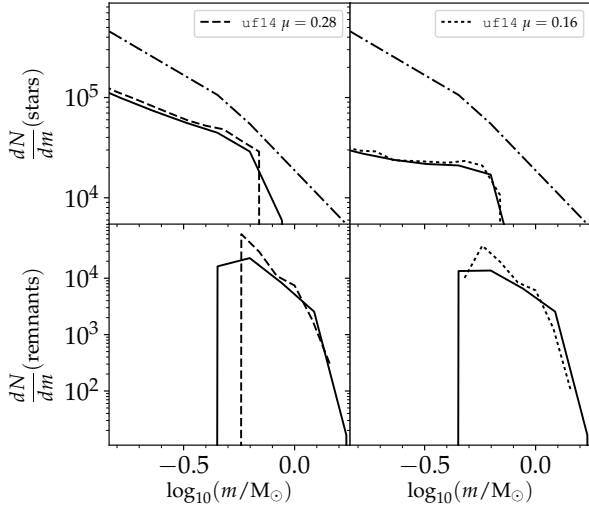


Figure 1. Comparison of the synthetic MF (solid lines) with the ufl4 model from Lamers et al. (2013). The top two panels show the visible stars at $\mu = 0.28$ (left) and $\mu = 0.16$ (right), where μ is the remaining mass fraction in the cluster. The dot-dashed line in both top panels is the IMF. The two bottom panels show the MF of the stellar remnants, compared at the same μ as before.

2.3 Escape

In the pre-collapse phase we assume that the escape rate is independent of stellar mass, i.e. $\dot{N}_j^s = N_j^s \dot{N}/N$ (similarly for \dot{N}_j^r), where \dot{N} is the total escape rate of the cluster which comes from EMACSS. After core collapse (also given by EMACSS) we apply an escape rate to each bin

$$\dot{N}_j^{\text{esc}} = \dot{N} \frac{N_j^s + N_j^r}{N} \frac{g(m_j)}{\sum_j g(m_j)} \quad (6)$$

where

$$g(m_j) = \begin{cases} 1 - (m_j/m_d)^{1/2}, & m_j < m_d, \\ 0, & m_j \geq m_d. \end{cases} \quad (7)$$

This simple functional form for \dot{N}_j^{esc} was found by matching the time derivatives of the functional forms for the MF as a function of time given by Lamers et al. (2013). With a value of $m_d \simeq 1.1 M_\odot$ we find a good agreement with results from N -body models (see example in Fig. 1). The 100% retention of stars and remnants more massive than m_d is becoming problematic when less than a few % of the initial mass is remaining, and hence this approximation is good enough for our purpose. The escape rate is divided over the stars and remnants as $\dot{N}_j^{\text{esc}} = \dot{N}_j^{\text{esc}} N_j^s / N_j$ (similarly for \dot{N}_j^{esc}), such that $\dot{N}_j^{\text{esc}} = \dot{N}_j^{\text{esc}} + \dot{N}_j^{\text{esc}}$.

2.4 Validation

To validate our implementation of the MF evolution we compare the predicted MF with one of the N -body simulations of Lamers et al. (2013). These simulations are setup with a Kroupa IMF (Kroupa 2001) and include stellar evolution. We find that our model provides an accurate description of the MF evolution in these simulations. In Fig. 1 we show a comparison of an N -body model with $N = 131\,072$ particles on a circular orbit at a radius of 8.5 kpc in

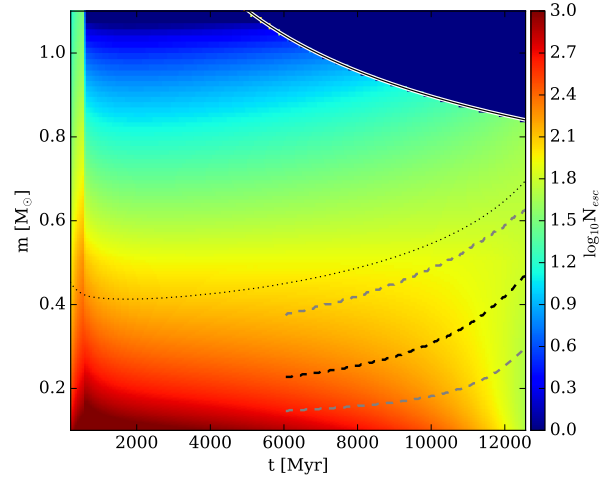


Figure 2. Number of escapers (colour coded in log-scale) as a function of time and mass for a simulated cluster with an initial mass of $2 \times 10^5 M_\odot$ on a circular orbit at a Galactocentric distance of 18 kpc (similar to Palomar 5). The solid line shows the main-sequence turn-off mass evolution, the dark dotted line is the median stellar mass remaining in the cluster and the dark dashed line is the median mass of the escaper stars while the grey dashed lines are mark the position of the first and third quartiles (i.e. 50% of the stars are between the grey lines).

a logarithmic potential. For illustrative purposes we compare our prediction with the N -body model at two different stages of dissolution $\mu = [0.16, 0.28]$, where μ is the remaining mass fraction of the cluster. We also show the predicted number of stellar remnants (mainly white dwarfs) compared to the N -body results (bottom panels). We observe that the visible stars are very well represented by our synthetic model with only minor deviations at the turn-off mass due to our approximation of the main-sequence lifetime. The remnant MF is in good general agreement considering the simplicity of our method.

Fig. 2 shows a summary of the escaper MF (EMF) evolution for a cluster that is near complete dissolution. We chose the initial conditions to reproduce the orbit of Palomar 5 (Küpper et al. 2015) and the initial mass such that full dissolution is at ~ 13 Gyr. Note that at ~ 500 Myr there is an abrupt change in the EMF, this happens at core-collapse where the preferential loss of low-mass stars starts to take place. Also, as the cluster approaches 13 Gyr, the median mass of escapers rises significantly, accounting to more than 50% of the stars above $0.45 M_\odot$ and 25% above $0.6 M_\odot$. This has important consequences for the visibility of streams, which we discuss in section 4.

3 MASS EVOLUTION IN THE GALAXY

The framework developed here allows us to predict the mass spectrum of escaped stars of a cluster given μ . Despite being a simple parametrisation, describing a cluster in terms of μ requires prior knowledge of its current mass (M), initial mass (M_i), and mass loss rate \dot{M} . Its current mass can be estimated from its integrated luminosity and/or kinematics, while M_i and \dot{M} require understanding of its orbital properties.

Here we adopt EMACSS in an iterative way to obtain M_i that correctly reproduces \dot{M} given its orbital properties. However, we need two missing ingredients, the cluster mass-loss history on eccentric orbits and its current mass-to-light ratio (Υ).

The version of EMACSS we use is unable to evolve a cluster on an eccentric orbit. To overcome this, we evolve the cluster on a circular orbit at a Galactocentric radius $R_{G,\text{eqv}}$, where the cluster has the same total lifetime. This is justified by the results of [Cai et al. \(2016\)](#) who showed that the evolution of M and r_h are similar for clusters on orbits with different eccentricities, but with the same dissolution time. This radius is given by ([Baumgardt & Makino 2003](#))

$$R_{G,\text{eqv}} = R_{\text{apo}}(1 - \epsilon), \quad (8)$$

where R_{apo} is the apocentre radius and ϵ is the orbital eccentricity. These parameters are obtained by the orbit integration procedure outlined in the section 3.1.

With an approximation for the mass loss in eccentric orbits at hand, we now need a prescription for Υ . Due to preferential loss of low-mass stars and stellar evolution, Υ evolves with time. Based on the work of [Anders et al. \(2009\)](#) we model Υ_V , i.e. the mass-to-light ratio using the luminosity in the V -band, as a linear function of the remaining mass in the cluster

$$\Upsilon_V = 0.8 + 1.2\mu_{\text{dyn}}. \quad (9)$$

Equation (9) gives $\Upsilon_V = 2$ if $\mu_{\text{dyn}} = 1$, which is consistent with a [Kroupa \(2001\)](#) IMF evolved to an age of 12 Gyr and $-2 \lesssim [\text{Fe}/\text{H}] \lesssim -1$ (e.g. [Bruzual & Charlot 2003](#); [Conroy & Gunn 2010](#)), while $\Upsilon_V \simeq 0.8$ if the remaining mass fraction approaches $\mu_{\text{dyn}} \simeq 0$. Note that in the N -body models of [Anders et al. \(2009\)](#) Υ_V increases again near dissolution, because then the GC consists of predominantly dark remnants, but this phase is short lasting hence we ignore it (but we note that NGC 6535 may be in this phase, [Halford & Zaritsky 2015](#)). Since [Anders et al. \(2009\)](#) evolves an aged IMF, their results isolate dynamical effects only. EMACSS, however, accounts for stellar evolution during the evolution of the cluster. In order to consistently use the [Anders et al. \(2009\)](#) relation, we assume the following relation $\mu = 2\mu_{\text{dyn}}$, which considers a 50% mass-loss due to stellar evolution. The assumption is reasonable for cluster older than ~ 10 Gyr, which is the case for most GCs in the MW

We proceed to use EMACSS to obtain the cluster initial mass. This is done by minimizing the absolute value of the difference between EMACSS predicted present-day mass and the cluster observed mass, where the observed luminosity is converted to mass using Eq. 9. The minimization procedure uses the Nelder-Mead simplex method with a tolerance of $1 M_\odot$.

EMACSS assumes a logarithmic Galactic potential, hence the mass evolution is most accurate where the rotation curve of the Galaxy is flat. In the innermost regions of the Galaxy (< 3 kpc) EMACSS will overestimate the mass loss, providing only a lower limit on the cluster remaining mass fraction. Clusters in the inner Galaxy will probe only a small fraction of the Galaxy volume, as well as having tidal tails that are more easily disrupted due to chaotic orbits and time-dependent potential from the bar ([Price-Whelan et al. 2016](#)), hence our approximation holds for most GCs of interest.

3.1 Orbit integration

The literature is rich regarding the measurement of GC proper motions (PMs), and for about 2/3 of the known cluster there is a measurement available. For almost all clusters a radial velocity mea-

surement is available. However, both these measurements are very heterogeneous.

We compiled a set of GCs from literature that have measured PMs. The sample was further expanded by using UCAC-4 absolute PMs by [Dambis \(2006\)](#), however, the uncertainties in this catalogue can be significant. The complete sample analysed here is shown in Table 1 where appropriate references are given for each individual object.

We carry out orbit integration using the popular galactic dynamics code GALPY ([Bovy 2015](#)). The Galaxy potential used is the MWPotential2014 which is composed of three components: a power-law with an exponential cut-off for the bulge, a [Miyamoto & Nagai \(1975\)](#) disk, and a [Navarro, Frenk & White \(1996\)](#) halo. We set the Sun's distance to the Galaxy centre to $R_\odot = 8.3$ kpc, its vertical offset to $z_\odot = 24.2$ pc, and its circular velocity to $V_c = 233$ km/s. The Solar reflex motion components adopted are the ones derived by [Schönrich et al. \(2010\)](#). We use the Dormand-Prince integration method ([Dormand & Prince 1980](#)). For the purpose of inferring orbital parameters, we integrate for 6 Gyr.

To propagate the uncertainties in position and velocity of each cluster we perform 1500 orbit realisations for each cluster. In each realisation we sample the values of PM from a normal distribution with a centre and dispersion given by the literature value and uncertainty respectively. We also assume a 5% uncertainty on the heliocentric distance to the cluster, we find that this assumption better encompasses the heterogeneous methodology for determining cluster distances (the uncertainty in distance is propagated to the total luminosity, as it depends on the distance modulus). We take the distance values and integrated V-band magnitude from the 2010 version of the Harris catalog ([Harris 1996, 2010](#)). At each realisation, the cluster initial mass, current mass and remaining mass-fraction is computed according to the recipe presented in this section. In addition to sampling the velocity and position uncertainties, we also sample from the cluster age and associated uncertainty. We take the ages from [VandenBerg et al. \(2013\)](#), and for cluster where no age is available we assume the mean age (11.9 Gyr) and dispersion (0.8 Gyr) of the full sample. Although there are age determination for a larger sample spread across the literature, we choose to use the largest one available in order to avoid any methodology biases.

With 1500 orbit samples we assume that the most representative value of R_{apo} , R_{peri} , ϵ , μ , and $M_{i,5}$ is given by the median of the distribution, while its uncertainty is given by the median absolute deviation (MAD). Our choice of median and MAD is motivated by the fact that the median is more sensitive to the asymmetries in the distribution while the MAD is less sensitive to outliers. By comparison with the more traditional mean and standard deviation we find that this approach gives more consistent results that are more representative of all clusters in our sample, in the sense that objects with very broad and asymmetric distributions have a median value that is more representative of the full sample. While clusters with double peaked distributions do not have a single peak favoured. This produces somewhat large MAD values for some clusters, however these will certainly encompass the most probable regions of parameter space.

To check the consistency of our orbit integration, we compare our eccentricity values with those in the axisymmetric case in [Moreno et al. \(2014\)](#). The comparison is restricted to clusters in common with their sample that use the same PM values, since we adopt more recent PM measurements for some of the clusters. In Fig. 3 we show the comparison with [Moreno et al. \(2014\)](#) (y -axis) and our eccentricity determination (x -axis). We flag outliers by selecting objects that lie more than 2 times the typical eccen-

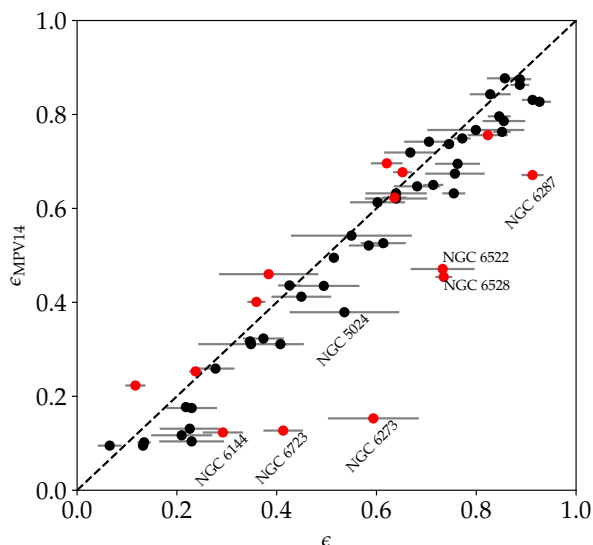


Figure 3. Comparison of the eccentricity obtained in this work (x -axis) with the ones obtained by (Moreno et al. 2014) using an axisymmetric potential (y -axis). Error-bars show the uncertainty in our measurements. Cluster in red have their current position within 3 kpc from the Galaxy centre, we indicate the names of those which deviate significantly from the identity.

tricity uncertainty. The bulk of the cluster lie along the identity line within the uncertainties. The outliers are clusters for which the orbit is strongly influenced by the bulge potential. Our central potential is slightly different than the one used by Moreno et al. (2014) which could be the source of the discrepancy.

In Fig. 4 we show one example of the orbital parameter exploration for Palomar 5. The diagonal plots show the 1D kernel density estimator (KDE) for each of the parameters sampled. The panels below the diagonal show the 2D KDE for each pair of parameters and the panels above show each individual sample. We also include the orbital phase ϕ which is computed using $\phi = (R_G - R_{\text{peri}})/(R_{\text{apo}} - R_{\text{peri}})$.

In order to get a complete picture of the Galactic GC system, we assume that GCs without PM measurements have an isotropic velocity distribution (hereby referred as the noPM sample). van den Bosch et al. (1999) show that in a logarithmic halo, a tracer population with density $\rho \propto r^{-\alpha}$ has a velocity dispersion $\sigma_{\text{GC}} = V_c/\sqrt{\alpha}$, and for the GCs $\alpha \simeq 3.5$ (Harris 1976). These clusters form about 1/3 of the sample and their orbits were sampled in the same fashion as before. However, we sample the velocities isotropically from a normal distribution with dispersion σ_{GC} . Cluster that fall in this category are indicated in Table 1. In addition to the clusters without PM, we moved two objects to the noPM sample, these are Terzan 8 and IC 4499. Their literature PM yielded unbound orbits, however, given that these come from the less accurate Dambis (2006) sample, we assume that this is due to measurement errors. Hence, had their PM removed from Table 1, and their orbits were sampled from the isotropic velocity distribution. We note that the clusters Pal 3, Rup 106, NGC 5634, IC 1257, and NGC 6426 have extremely high R_{apo} , which is likely due to inaccuracies in their PM measurement. However, since we were able to recover bound orbits, we choose to keep these objects in our sample. We also include a derivation of the Jacobi radius (r_J) for each cluster at their current position. We use the King (1962) formula and use our derived present-day mass to propagate the uncertainty to r_J .

In Fig. 5 we show the resulting distributions of R_{apo} and μ .

We note that GCs closer to dissolution (low μ) tend to have smaller R_{apo} , i.e. clusters closer to the Galactic centre where the tidal field of the bulge is strong, while clusters with higher μ span a wider range of R_{apo} . Cluster also have a maximum $\mu \sim 0.55$ which is due to the fast mass loss from stellar evolution that remove about half of M_i at an age of ~ 12 Gyr. We mark regions of parameter space that are more extreme than what is observed for Palomar 5 (i.e. closer to disruption and/or with a larger R_{apo}). This selection is motivated by the usefulness of streams as tracers of the potential beyond 20 kpc. Based solely on these parameters and μ , we expect clusters in the *green* region of the parameters space to be good candidates for tidal tail search. These cluster are AM4, Palomar 1, Palomar 7 (IC 1276), and Whiting 1. Of these clusters, only Palomar 1 has reported tidal tails (Niederste-Ostholt et al. 2010). These clusters are also at large heliocentric distances which makes obtaining PMs more difficult and only Palomar 7 has measured PMs. The noPM sample cluster mentioned above, despite having low uncertainties in μ and R_{apo} , may suffer from additional biases and their location in this plane is not as reliable as for the PM sample, hence our estimates may not hold once PM becomes available for these objects.

We note that our cluster mass estimates are based on the assumption of a static MW potential, in the sense that all cluster orbit the same potential – and on a given orbit – during their whole lifespan. In comparison to the real orbital history of a cluster, our estimates may yield discrepant results. If we would account for the secular growth of the Milky Way, we would find μ values that are slightly higher because the average tidal field experienced in the past is weaker (Renaud & Gieles 2015). Accreted clusters from minor or major merger events could have been in radically different environments for a significant fraction of time (Renaud, Agertz & Gieles 2017). This would ultimately leave an imprint on the cluster evolution such as a present day mass function (PDFM) that is not consistent with its current orbit.

With the properties of the orbits and μ for all GCs, we now discuss the visibility of streams in the next section.

4 THE VISIBILITY OF A STREAM

We have established that the cluster dissolution stage is a major factor in the typical mass of the stars in the stream. Nonetheless, it is known that streams are in their most densely packed stage near R_{apo} . So we expect that the most easily detectable streams are those from clusters with low μ (i.e. near dissolution) and high ϕ (i.e. near R_{apo}).

In Fig. 6 we show the distribution of μ and ϕ for all clusters, except those in the noPM sample, since these have unreliable values of ϕ . We split the sample into clusters that have $R_{\text{apo}} > 10$ and < 10 kpc. We highlight Palomar 5 (Odenkirchen et al. 2001), NGC 5897 (Adrian Price-Whelan private communication), and NGC 5466 (Belokurov et al. 2006; Grillmair & Johnson 2006) since these clusters have tidal tails detected in SDSS or Pan-STARRS. Recently, tidal tails have been found around the clusters NGC 7492, Eridanus, and Pal 15 (Navarrete et al. 2017; Myeong et al. 2017), however, these can not be used in our comparison as no PM measurements are available. For those with $R_{\text{apo}} > 10$ kpc we show the two lowest μ values (green) and the two highest ϕ values (red). These objects are high-probability clusters for detection of streams considering SDSS-like photometric performance.

The cluster NGC 5466 seems to be an exception, in the sense that it should not have easily detectable tails based on its relatively

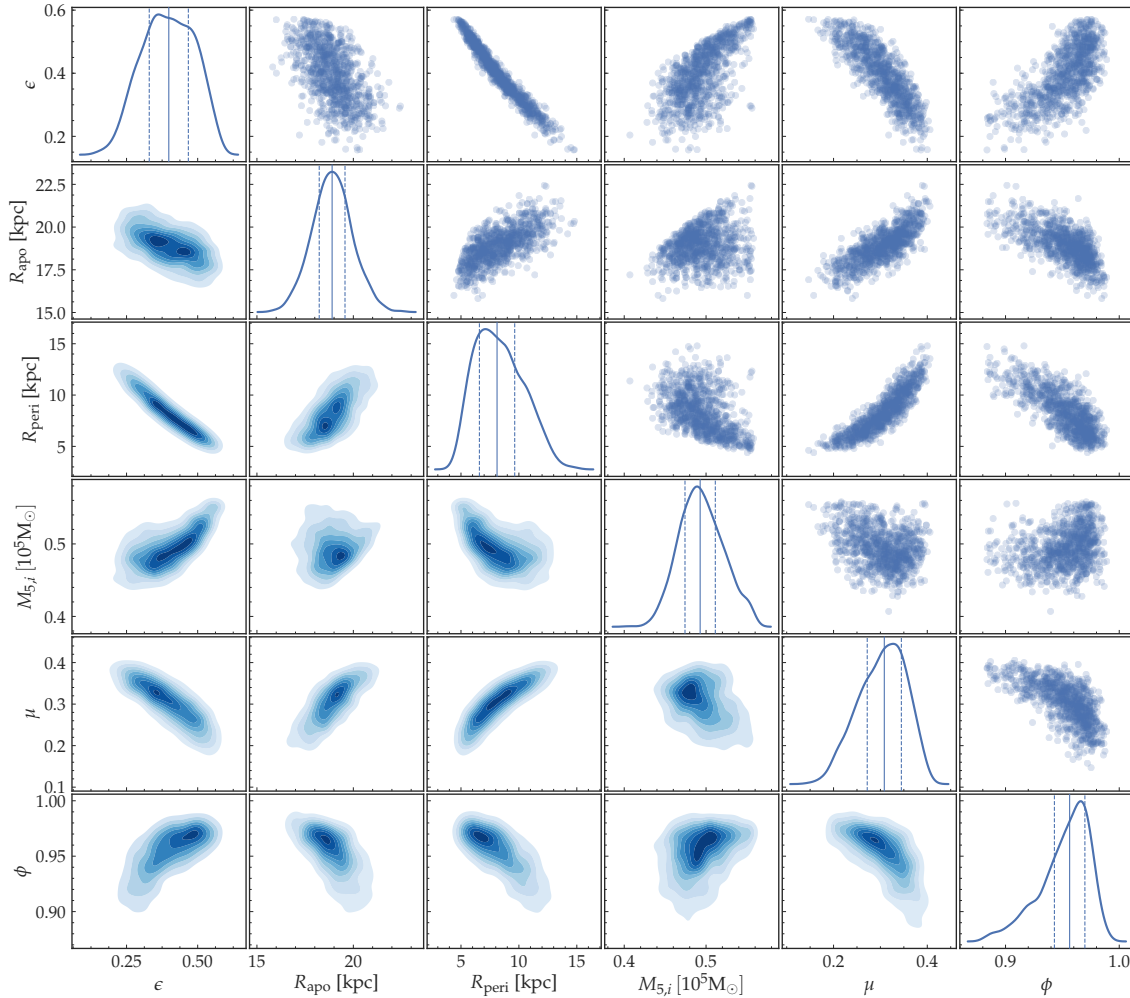


Figure 4. Summary plot showing the relation among all parameters explored in the orbit integration of Palomar 5 as an example. Panels below the diagonal show the 2D kernel density estimator for the samples, panels above the diagonal show the individual samples, and the diagonal shows the 1D kernel estimator with median (solid line) and MAD (dashed line) indicated.

high μ and being near R_{peri} , but [Belokurov et al. \(2006\)](#) detected a 4° tail around this cluster using SDSS data, followed by [Grillmair & Johnson \(2006\)](#) who detected it up to 45° . We point out that NGC 5466 is a cluster that has an PDMF that is depleted in low-mass stars ([Sollima et al. 2017](#)) and it has been suggested by [Webb et al. \(2017\)](#) that this cluster is not mass segregated. According to our prediction, NGC 5466 should have a pristine PDMF since $\mu \simeq 0.5$. Interestingly, the cluster is also on a retrograde, high eccentricity orbit ([Forbes & Bridges 2010](#)), which is a strong indication for it being an accreted cluster. Here we strengthen the suspicion about its accreted origin, since it has an PDMF inconsistent with its orbital history which could be the effect of a stronger tidal field in the past, perhaps from its original host galaxy.

As shown in Fig. 6, the two clusters that are closest to the optimal detectability conditions (low μ and high ϕ) and have $R_{\text{apo}} > 10$ kpc are NGC 288 and NGC 6341 (M92). The former has weak signs of tidal tails ([Grillmair et al. 2004](#)) in shallow IR data, while the latter has signs of extra-tidal structure ([Lee et al. 2003](#)). We also highlight two clusters that are close to disruption and have $R_{\text{apo}} > 10$ kpc, which are IC 1276, also known as Palomar 7, and NGC 6779 (M56). However, both clusters are quite close to the bulge in projection ($|b| < 6^\circ$), which will likely introduce differ-

tial reddening effects and a high surface density of field stars which can make stream detection challenging.

The criteria for being an optimal target for finding tidal tails appears to yield consistent predictions, at least based on the present literature. We stress, however, that each cluster is a particular case in the sense that its distance, field contamination, and orbit projection should be considered since these factors may produce non-trivial observing conditions. For instance, the cluster M92 is an optimal candidate, however its proximity to the Sun will lower the projected surface density. With such complications in mind, our predictions should be taken as general constraints that can be used as guidelines for future observations and follow-ups.

Finally, this framework can be used to predict not only the spectral properties of stream stars (colours and magnitudes), but also their distribution in PM space of stream stars. With the velocity information, disentangling field stars from stream stars will be much more efficient than current photometry-based methods. This may allow the study of streams in the inner Galaxy, provided extinction is not an issue.

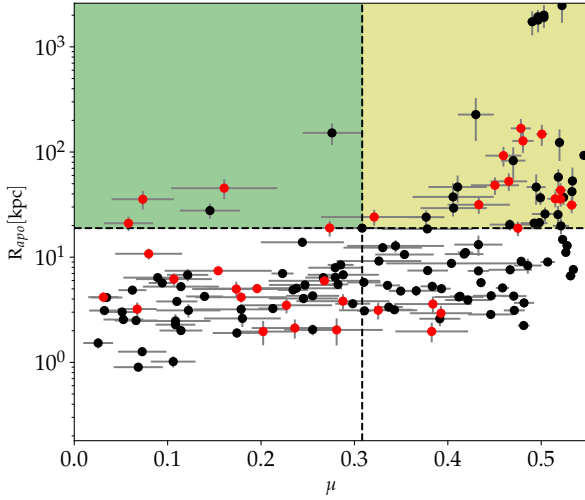


Figure 5. Distribution of μ and R_{apo} . Errorbars were computed using the MAD estimator. Red circles are cluster from the noPM sample. The green shaded region show cluster that have both orbital parameters more extreme than Palomar 5, while the yellow shaded region show clusters that have a R_{apo} larger than Palomar 5. The clusters in the green region are AM 4, Palomar 1, Palomar 7 (IC 1276), and Whiting 1. Note that the maximum $\mu \simeq 0.55$ is because all GCs have lost about 45% of their initial mass as the result of stellar evolution.

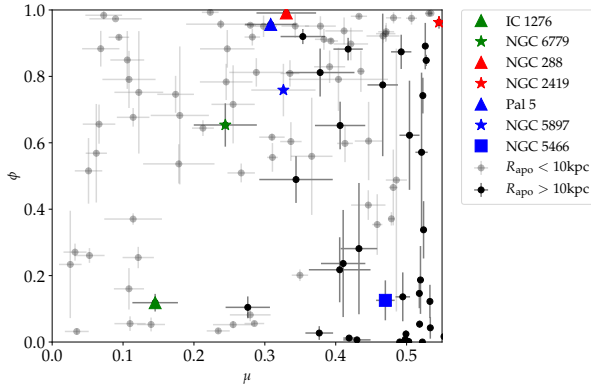


Figure 6. Remaining mass μ against orbital phase ϕ (1 at apocentre), excluding the noPM sample. In grey we show cluster with $R_{\text{apo}} < 10$ kpc, and in black cluster with $R_{\text{apo}} > 10$ kpc. Error-bars are derived from the MAD estimator. Cluster with detected tidal tails are marked in blue. From the cluster with $R_{\text{apo}} > 10$ kpc we highlight the two closest to disruption (green symbols) and the two closest to apocentre (red symbols).

5 THE CASE OF PALOMAR 5

Using the information about the remaining mass in a given cluster and its orbital history we are able to track the masses of the particles that leave the cluster. However, we still need a realistic way of simulating the ejection mechanism and produce a tidal tail.

In a cold stream self-gravity is not important. This greatly simplifies the stream simulation in the sense that one only needs to integrate individual orbits of particles being *sprayed* off a progenitor in a static potential to produce a realistic stream. This class of codes became known as spray-particle methods and has been explored in many successful applications (Küpper et al. 2012; Fardal et al. 2015; Sesar et al. 2015; Erkal et al. 2016; Amorisco 2015; Bonaca et al. 2014). Despite the simplicity, this method still re-

quires prescriptions for how particles are ejected from the progenitor. We refer to Fardal et al. (2015) for a comprehensive comparison of methods.

In this work, we adopt the spray-particle implementation by Küpper et al. (2012). The escape velocity of stars was modelled based on an extensive study of N -body simulations in tidal fields presented by Claydon, Gieles & Zocchi (2016). These authors studied so-called ‘potential escapers’ in their simulations, which are stars that are energetically unbound, but still associated with the cluster. From this, and theoretical arguments, they find that the velocity dispersion of these stars near the Jacobi radius (r_J) can be approximated by

$$\sigma_J \simeq 0.9 \text{ km s}^{-1} \left(\frac{M}{10^5 M_\odot} \right)^{1/4} \left(\frac{R_G}{5 \text{ kpc}} \right)^{-1/3}. \quad (10)$$

The approximation above is valid for circular orbits. In order to use it for eccentric orbits we find the circular orbit that has the same life-time given by equation (8).

The release mechanism adopted here assumes a Maxwellian velocity distribution for the escapers with the characteristic velocity scale equal to σ_J . Particles are ejected from the Lagrange points plus a random offset given by a $0.3r_J$ dispersion normal distribution. The extra offset in position is required to match N -body simulations (Küpper et al. 2012; Lane et al. 2012; Bonaca et al. 2014; Fardal et al. 2015; Pearson et al. 2015).

Each particle from the simulated tidal stream represents an ensemble of stars with a known MF (i.e. given by the moment the particle escaped the cluster and the algorithm of section 2). Combining this information with a mass-luminosity relation we can produce an expected luminosity function (LF) for each particle in the simulation. For Palomar 5 we choose an 11 Gyr isochrone (Bresnan et al. 2012)² with a metallicity of $[\text{Fe}/\text{H}] = -1.4$ (Koch et al. 2004). To simulate SDSS-like photometry we use a faint magnitude limit in the g -band of 22.5. Each tail particle has its associated EMF integrated from the turn-off mass to the mass that corresponds to the chosen magnitude limit, taking into account the heliocentric distance to each individual particle. The result is a list of particles with on-sky positions and a weight that is proportional to the number of observable stars it represents. We produce density maps by counting stars in bins on the sky and dividing by the solid angle of each bin.

To illustrate the effects of the MF evolution on the detectability of Palomar 5’s stream we perform two simulations. Both in the same orbit, but with one that is consistent with the lower limit of its present-day mass of $4500 M_\odot$ (Odenkirchen et al. 2002) and another which has a current mass that is roughly 3 times higher ($12000 M_\odot$). To artificially increase its current mass, we increase its observed luminosity and run through our μ estimate method described in Section 3.1.

Tidal tails are sparse structures and to estimate the detectability of a given stream one must consider the effect of overlapping field stars. To estimate the contribution of field stars we analyse a 4 deg^2 patch of the sky observed by SDSS. We filter stars in colour and magnitude according to the best-fit isochrone in literature (Koch et al. 2004). We select stars with colours $(g-r) \pm 1.5\sigma_{g-r}(g)$ away from the isochrone, where $\sigma_{g-r}(g)$ is the typical colour uncertainty at a given magnitude g . We apply the same g -band cut-off at $g = 22.5$ as before. In the patch of the sky analysed this yields a mean density of $0.058 \text{ stars/arcmin}^2$ which was

² http://stev.oapd.inaf.it/cgi-bin/cmd_2.8

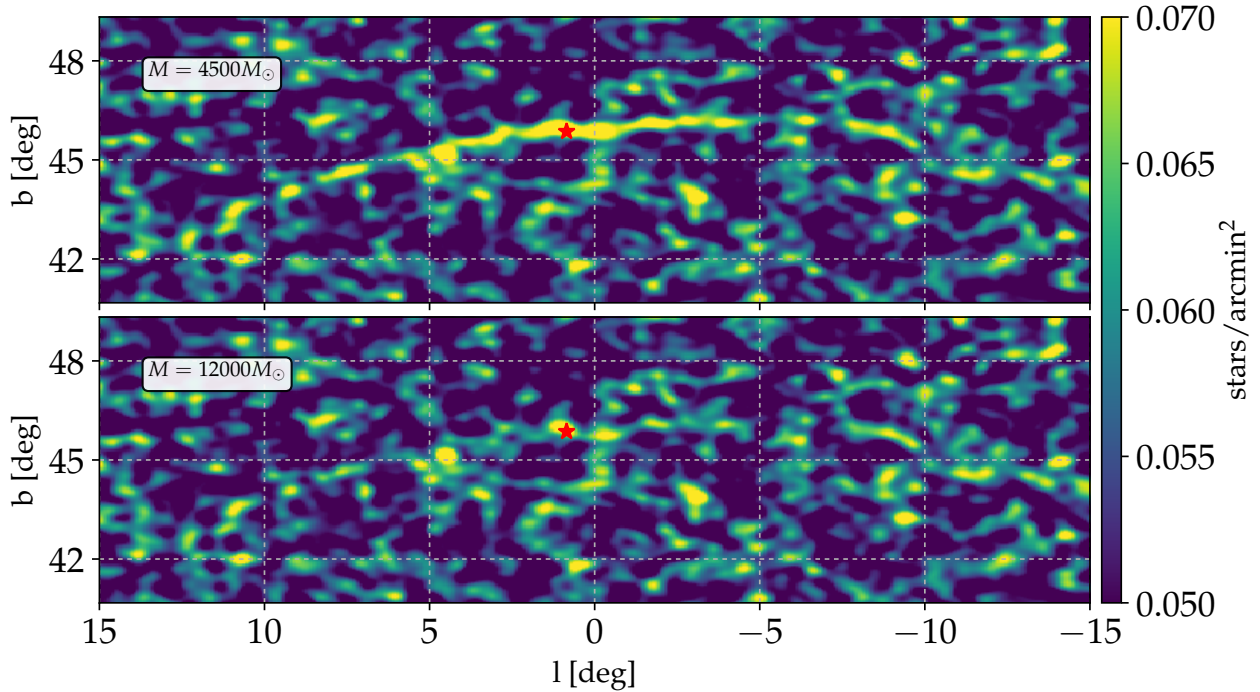


Figure 7. Two simulations of Palomar 5 tidal tails. The top panel show a Palomar 5 that is close to its estimated present-day mass (Odenkirchen et al. 2001) while the bottom panel it is presently ~ 3 times more massive. The red star symbol marks the position of the cluster.

used to generate a homogeneous distribution in the region around the Palomar 5. This approach does not account for variations in the number of field stars with e.g. galactic latitude, however it is representative of the field stars density in the vicinity of the cluster. It is also a first order approximation of the traditional matched-filter approach used to detect streams (Odenkirchen et al. 2001; Balbinot et al. 2011), in the sense that it selects only stars with colours consistent with the cluster population.

In Fig. 7 we show the predicted density of stars for the two simulated Palomar 5 tails. The present-day mass is indicated in each panel. Field stars were added as described above and both maps are smoothed using a Gaussian kernel with 0.075 deg dispersion. We notice that the model with the mass in agreement with observations shows more prominent tails that are clearly visible in the range $-5^\circ < l < 5^\circ$. Also the trailing tail (positive l) appears slightly more extended, which is also confirmed by Pan-STARRS observations (Bernard et al. 2016). The average density of the stream plus background is of 0.069 stars/arcmin 2 , which is in agreement with SDSS data (Odenkirchen et al. 2001). We note, however, that some of the fainter stream features are somewhat dependent on the random background realisation. The more massive simulation has a mean density $\sim 20\%$ lower than the normal mass one, even though its mass loss rate is $\sim 30\%$ higher. The density decrease makes most of the stream fall below the background level. The different density can be explained by the median mass of stream stars: the stars in the realistic Pal 5 stream simulation have a median mass of $0.3 M_\odot$, while only $0.22 M_\odot$ in the massive one.

Finally, we compare our stream prediction to SDSS data. We use the matched-filter density map from Balbinot et al. (2011); Küpper et al. (2015) which follows closely the methodology outlined by Odenkirchen et al. (2001), the discovery paper. For a fair comparison between SDSS matched-filtered data and our simulated stream plus background we must take into account that the

matched-filter has a higher efficiency in classifying stream stars. We assume that field stars that fall within the isochrone defined colour-magnitude mask – discussed above – are discarded with a 50% efficiency. Effectively, this is the equivalent of lowering the background level by 50%.

In Fig. 8 we show our matched-filter equivalent density map for the $4500 M_\odot$ simulation. The overlaid contours are from Balbinot et al. (2011) and Küpper et al. (2015), where we show the detection confidence levels from 1 to 5σ . The shaded region marks regions where the SDSS footprint becomes patchy and/or too close to the bulge causing spurious detections. Notice that the modelled stream is in very good agreement with the observational data. Most notably it reproduces the length on the stream main body and some of the over/under dense regions. We note that the length is reproduced even if we assume a matched-filter decontamination efficiency up to 80%. Despite the very good agreement, we stress that some of the features observed are dependent on the background realization, indicating that these are close to the noise level. As pointed out by Thomas et al. (2016) some of the features observed in SDSS do not stand the trial of deeper photometric data.

Even though the comparison with SDSS show great potential, we leave a more detailed analysis of Palomar 5 for future works where we explore in more detail its stream properties. For instance, we do not explore different methods of stream generation, N -body simulations or a more detailed projection onto observational space (e.g. completeness, source miss-classification, etc). The goal of this work is to illustrate the nuances generated by collisional dynamics and their overall impact on stream properties.

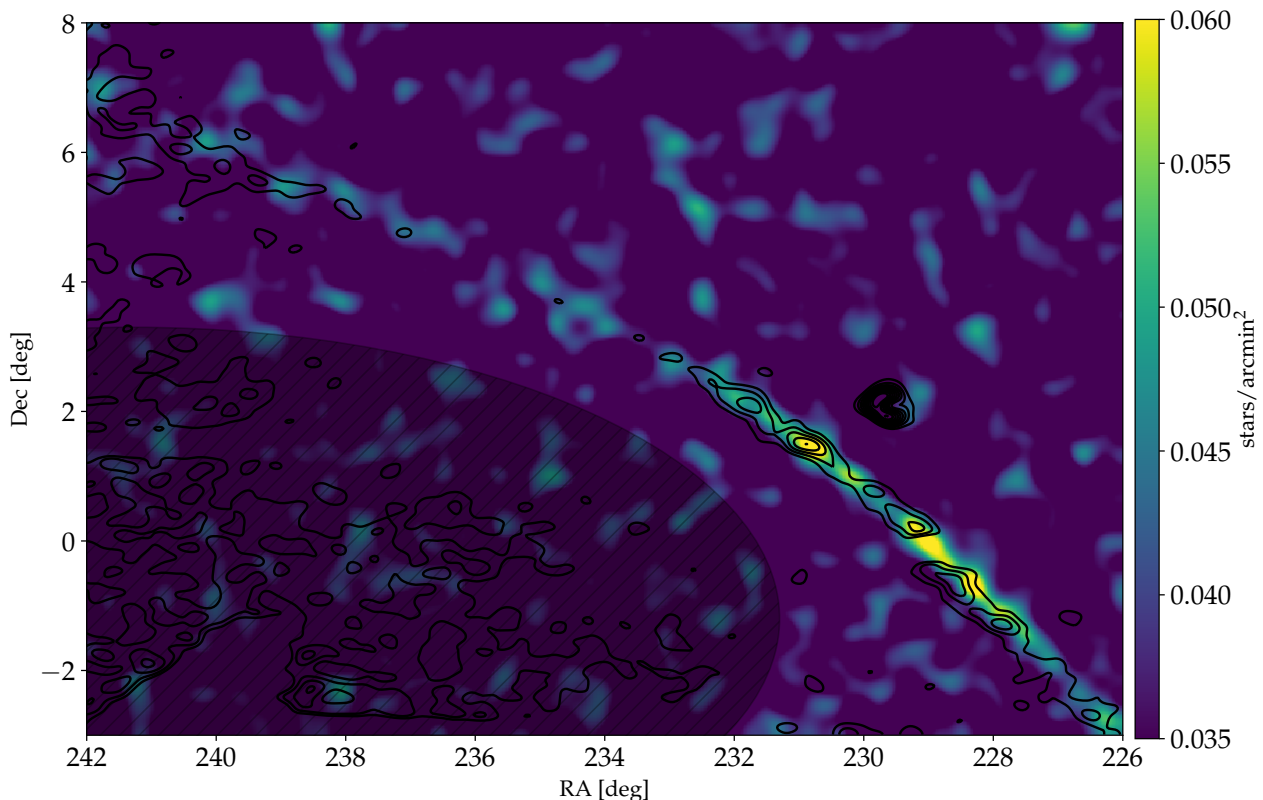


Figure 8. The same simulation of Palomar 5 as shown in the top panel of Fig. 7 where the background has been lowered to a level consistent with the decontamination efficiency of the matched-filter technique. Contours are the 1,2,3,4, and 5 σ confidence levels of the SDSS detection, based on the work of Balbinot et al. (2011); Küpper et al. (2015). The shaded region delimits a portion of the sky where contamination by the bulge becomes important and the SDSS contours are unreliable. The contour blob at $(\alpha, \delta) \simeq (230, 2)$ is the foreground cluster M5.

6 CONCLUSION

We present a method for taking into consideration the internal evolution of a cluster due to collisional dynamics on the formation of cold streams. This method uses the code EMACSS (Alexander et al. 2014) to simulate the cluster main properties such as total bound mass, number of stars, and mass-loss rate. We couple this information to a algorithm that evolves the MF based on simplified version of the method presented in Lamers et al. (2013).

The median mass of the escaping stars is always below the median mass of the bound stars, and the mass of escapers gradually increases as the evolution proceeds. Our predictions for the evolution of the mass function of stars and stellar remnants are in good agreement with results of an N -body model.

Using position and velocity information for MW GCs we derive orbital parameters and their uncertainties. These were coupled to a simple mass-loss prescription to infer the cluster remaining and initial masses, effectively allowing us to assess the current stage of dissolution of each cluster. We validate our orbit integration by comparing it to the sample of Moreno et al. (2014), which we find to be in good agreement.

As a test case, we show a detailed simulation of the cluster Palomar 5. We use the same spray particle code used in Küpper et al. (2015) with the additional prescription presented in Claydon et al. (2016) for the velocity dispersion of escaper stars. We generate two streams, a ‘normal’ one which is consistent with the cluster present-day mass, and an ‘overweight’ one which yields a cluster that is 3 times more massive today. We find that the ‘normal’ mass

simulation successfully predicts the surface density of stream stars as observed by SDSS, as well as some of the features in the stream (asymmetry and some over-densities). On the other hand, the ‘overweight’ simulation yields a stream that is below the SDSS detection limit throughout most of its extension. The simulations presented here by no means intend to be an exhaustive exploration of Palomar 5 stream structure. We suggest the works by Pearson et al. (2015), Küpper et al. (2015), and Price-Whelan et al. (2016) for a detailed treatment of stream formation and structure in a variety of scenarios.

We use Palomar 5, and other clusters with detected streams in SDSS or Pan-STARRS, as a guideline to probe properties that enhance the probability of stream detection. As demonstrated, most cluster with stream are close to dissolution and/or have atypical PDMFs (Webb et al. 2017). We also find that these clusters are more likely to be close to apocentre as well, a phase where stream stars are in their most densely packed configuration. From the sample with PM we single out the clusters NGC 288 and NGC 6341 (M92) as the next best candidates after Palomar 5, to have detectable tidal tails. Indeed there is evidence in literature for this (Lee et al. 2003; Grillmair et al. 2004). From the noPM sample, we highlight the clusters AM4, Palomar 1, Palomar 7, and Whiting 1. These clusters have R_{apo} larger than 18 kpc and are closer to dissolution than Palomar 5. Among these clusters, only Palomar 1 has evidence for tidal tails (Niederste-Ostholt et al. 2010), although wide-field data is lacking for the other three.

Peebles (1984) suggest that GCs form in small dark matter halos, and if these are still surrounding the cluster, they prevent

stars from escaping. [Moore \(1996\)](#) argues that the presence of tidal tails near some GCs and dwarf galaxies implies that these objects can not have a massive dark matter halo. This argument could be turned around to use the absence of tails near massive GCs (e.g. [Kuzma et al. 2016](#)) as evidence for the presence of a dark matter halo. Our results provide a more natural explanation for the absence of tidal streams near massive GCs, despite their higher mass loss rate (at a given orbit).

The overall distribution of cluster orbital properties shows how rare objects like Palomar 5 are, and certainly provide a dire perspective for the use of cold streams to probe the halo beyond 18 kpc. However, progenitor-less streams outnumber those associated with GCs (for recent discoveries see [Bernard et al. 2016](#)), offering hope for probing the halo at larger distances. Although, the number of cluster close to disruption in the outer halo is expected to be low. [Contenta et al. \(2017\)](#) recently showed that the number of cluster close to disruption at Galactocentric radius between 20 and 150 kpc is $3.3^{+7.7}_{-1.6}$. However, there may be a larger population of progenitor-less streams, if the orbital phase mixing time is long. Also, some of the low-mass cluster in the outer halo show signs of streams, such as Willman 1 ([Willman et al. 2006](#)), Balbinot 1 ([Bernard et al. 2016](#)), Segue 1 ([Niederste-Ostholt et al. 2009](#)), and Hercules ([Küpper et al. 2017](#)).

Upcoming surveys such as the Large Synoptic Survey Telescope (LSST [LSST Dark Energy Science Collaboration 2012](#)) will greatly increase sky coverage and photometric depth, potentially revealing many new streams. However, greater photometric depth comes at the cost of an increase density of field stars and background galaxies. Next generation detection methods must account for this and devise ways of better modelling the stream as well as background. The addition of velocity information will certainly help disentangling stream stars from field stars, and the next data release of Gaia will provide a unique test case for new methods.

ACKNOWLEDGMENTS

We thank Holger Baumgardt for kindly providing NBODY model used in this work and Andreas Küpper for providing the streakline code. MG thanks the Royal Society for financial support (University Research Fellowship) and both authors acknowledge financial support from the European Research Council (ERC-StG-335936, CLUSTERS). Both authors thank Justin Read and Jeremy Webb for interesting discussions and suggestions.

SDSS-III is managed by the Astrophysical Research Consortium for the Participating Institutions of the SDSS-III Collaboration including the University of Arizona, the Brazilian Participation Group, Brookhaven National Laboratory, Carnegie Mellon University, University of Florida, the French Participation Group, the German Participation Group, Harvard University, the Instituto de Astrofísica de Canarias, the Michigan State/Notre Dame/JINA Participation Group, Johns Hopkins University, Lawrence Berkeley National Laboratory, Max Planck Institute for Astrophysics, Max Planck Institute for Extraterrestrial Physics, New Mexico State University, New York University, Ohio State University, Pennsylvania State University, University of Portsmouth, Princeton University, the Spanish Participation Group, University of Tokyo, University of Utah, Vanderbilt University, University of Virginia, University of Washington, and Yale University.

Name	μ_α	μ_δ	V_{los}	R_{apo}	R_{peri}	ecc	M_i	μ	ϕ	r_J	Refs
	mas/yr	mas/yr	km s ⁻¹	kpc	kpc		10 ⁵ M _⊙			pc	
NGC 104	5.64±0.2	-2.02±0.2	-18.0±0.1	7.63±0.02	5.85±0.1	0.13±0.01	18.89±1.24	0.53±0.01	0.99±0.01	137.45±3.39	3
NGC 288	4.67±0.42	-5.62±0.23	-45.4±0.2	12.32±0.21	2.72±0.59	0.64±0.06	2.05±0.08	0.33±0.04	0.99±0.01	76.43±4.02	1,3
NGC 362	5.07±0.71	-2.55±0.72	223.5±0.5	10.69±0.47	0.84±0.2	0.86±0.04	8.51±0.52	0.42±0.02	0.88±0.03	112.06±4.57	3
Whiting 1*	–	–	–	46.22±10.17	20.64±6.36	0.41±0.11	0.06±0.01	0.17±0.05	0.5±0.31	37.56±2.28	–
NGC 1261	1.33±0.89	-3.06±1.06	68.2±4.6	25.54±3.74	5.72±2.17	0.65±0.06	4.41±0.27	0.5±0.01	0.63±0.16	146.38±6.31	8
Pal 1*	–	–	–	21.72±3.85	9.7±3.4	0.41±0.12	0.13±0.04	0.06±0.03	0.6±0.29	22.59±2.13	–
AM 1*	–	–	–	155.74±27.37	55.06±27.66	0.52±0.17	0.27±0.02	0.48±0.01	0.65±0.27	203.08±9.32	–
Eridanus*	–	–	–	119.12±22.17	43.68±21.38	0.5±0.17	0.38±0.03	0.48±0.01	0.64±0.28	191.61±8.84	–
Pal 2*	–	–	–	41.88±5.86	13.7±7.14	0.52±0.18	5.06±0.34	0.52±0.01	0.75±0.22	242.15±9.84	–
NGC 1851	1.28±0.68	2.39±0.65	320.5±0.6	37.02±5.79	6.59±1.17	0.71±0.02	6.99±0.44	0.52±0.01	0.34±0.09	166.46±6.04	1,3
NGC 1904	2.12±0.64	-0.02±0.64	205.8±0.4	21.07±0.79	5.44±1.7	0.59±0.09	4.69±0.3	0.49±0.01	0.87±0.05	153.79±6.0	2,3
NGC 2298	4.05±1.0	-1.72±0.98	148.9±1.2	18.59±1.12	5.29±1.84	0.56±0.11	1.29±0.1	0.38±0.05	0.81±0.07	81.27±4.08	2,3
NGC 2419	-0.17±0.26	-0.49±0.17	-20.2±0.5	92.19±2.93	30.77±13.47	0.5±0.16	18.88±1.21	0.55±0.01	0.97±0.01	719.16±30.56	8
Pyxis*	–	–	–	50.72±8.33	18.25±8.51	0.51±0.15	0.68±0.05	0.46±0.02	0.69±0.25	132.14±6.52	–
NGC 2808	0.58±0.45	2.06±0.46	101.6±0.7	12.89±0.37	2.42±0.38	0.68±0.05	18.52±1.17	0.53±0.01	0.85±0.02	176.87±6.28	5
E 3	-7.09±1.73	3.38±1.92	99.0±99.0	10.88±1.28	4.49±1.56	0.44±0.14	0.47±0.14	0.08±0.03	0.73±0.21	24.59±2.04	8
Pal 3	0.33±0.23	0.3±0.31	83.4±8.4	2053.2±462.51	94.05±3.22	0.91±0.02	0.63±0.04	0.5±0.01	0.0±0.01	234.07±10.37	8
NGC 3201	5.28±0.32	-0.98±0.33	494.0±0.2	21.34±0.99	9.0±0.08	0.41±0.02	3.17±0.2	0.5±0.01	0.01±0.01	83.46±2.35	5
Pal 4*	–	–	–	140.18±25.72	46.43±23.97	0.53±0.18	0.84±0.06	0.5±0.01	0.67±0.27	283.04±12.73	–
NGC 4147	-2.08±0.48	-3.07±0.46	183.2±0.7	29.31±2.12	7.02±2.05	0.62±0.08	1.09±0.06	0.41±0.03	0.65±0.07	95.97±5.03	3
NGC 4372	-6.49±0.33	3.71±0.32	72.3±1.2	7.41±0.06	2.99±0.11	0.43±0.01	4.59±0.26	0.43±0.01	0.98±0.01	77.82±2.31	5
Rup 106	-6.55±1.07	0.72±1.13	-44.0±3.0	1946.97±290.22	18.47±0.69	0.98±0.01	1.16±0.08	0.5±0.01	0.0±0.01	96.01±4.8	8
NGC 4590	-3.76±0.66	1.79±0.62	-94.7±0.2	36.7±5.23	9.66±0.31	0.58±0.04	2.94±0.19	0.5±0.01	0.02±0.01	88.54±3.36	2,3
NGC 4833	-8.11±0.35	-0.96±9.34	200.2±1.2	8.57±0.44	0.98±0.54	0.8±0.1	7.11±0.69	0.38±0.06	0.82±0.06	85.12±3.55	5
NGC 5024	0.5±1.0	-0.1±1.0	-62.9±0.3	55.37±17.46	16.85±0.93	0.54±0.11	9.79±0.67	0.53±0.01	0.04±0.03	199.02±8.8	3
NGC 5053	-1.89±1.23	-0.39±1.95	44.0±0.4	19.84±1.9	8.86±3.42	0.42±0.12	1.77±0.11	0.46±0.02	0.85±0.14	103.63±4.91	8
NGC 5139	-5.08±0.35	-3.57±0.34	232.1±0.1	6.65±0.03	0.97±0.04	0.75±0.01	41.19±2.54	0.53±0.01	0.99±0.01	161.71±3.66	2,3
NGC 5272	-1.1±0.51	-2.3±0.54	-147.6±0.2	14.75±0.63	5.03±0.95	0.49±0.07	11.61±0.75	0.52±0.01	0.74±0.05	158.64±5.67	3
NGC 5286	-5.09±0.92	-1.2±0.88	57.4±1.5	8.99±0.28	4.76±0.96	0.3±0.09	10.28±0.63	0.51±0.01	0.98±0.02	121.62±5.16	8
AM 4*	–	–	–	36.94±7.98	16.91±5.48	0.41±0.12	0.06±0.02	0.08±0.03	0.49±0.3	25.0±2.11	–
NGC 5466	-4.65±0.82	0.8±0.82	110.7±0.2	80.14±25.9	6.77±1.08	0.85±0.02	2.1±0.12	0.47±0.01	0.13±0.06	105.03±4.52	3
NGC 5634	-5.3±3.02	-0.65±2.12	-45.1±6.6	2470.22±697.16	21.01±0.72	0.98±0.01	3.87±0.23	0.52±0.01	0.0±0.01	158.46±6.69	8
NGC 5694*	–	–	–	34.32±4.79	11.46±5.85	0.53±0.18	4.47±0.29	0.51±0.01	0.76±0.21	203.68±9.94	–
IC 4499*	–	–	–	18.4±2.57	6.38±3.28	0.49±0.18	2.94±0.23	0.47±0.02	0.75±0.21	112.86±6.44	8
NGC 5824*	–	–	–	30.21±4.19	9.82±5.21	0.53±0.18	11.26±0.73	0.53±0.01	0.77±0.2	258.04±12.75	–
Pal 5	-2.39±0.17	-2.36±0.15	-58.7±0.2	18.9±0.66	8.16±1.42	0.4±0.07	0.49±0.02	0.31±0.03	0.96±0.01	60.89±3.31	9
NGC 5897	-4.93±0.86	-2.33±0.84	101.5±1.0	9.26±0.79	1.87±0.51	0.67±0.05	3.18±0.17	0.33±0.04	0.75±0.07	62.99±4.14	2,3
NGC 5904	5.07±0.68	10.7±0.56	53.2±0.4	57.57±10.7	3.43±0.13	0.89±0.02	10.93±0.67	0.52±0.01	0.05±0.01	100.52±2.97	11
NGC 5927	-5.72±0.39	-2.61±0.4	-107.5±0.9	5.1±0.16	4.47±0.12	0.07±0.02	4.57±0.27	0.46±0.01	0.35±0.09	58.79±1.77	5
NGC 5946	-4.39±0.3	-6.01±0.26	128.4±1.8	6.83±0.41	1.46±0.32	0.65±0.05	3.28±0.06	0.29±0.04	0.81±0.04	52.05±3.31	8
NGC 5986	-3.81±0.45	-2.99±0.37	88.9±3.7	5.09±0.26	0.23±0.06	0.91±0.02	11.65±1.03	0.25±0.04	0.96±0.01	66.05±4.83	5
Pal 14*	–	–	–	88.01±15.42	33.71±15.68	0.48±0.16	0.29±0.02	0.46±0.02	0.64±0.28	141.39±7.14	–
Lynga 7*	–	–	–	4.99±0.44	1.48±0.64	0.55±0.15	2.35±0.35	0.2±0.05	0.83±0.13	34.39±1.79	–
NGC 6093	-3.31±0.58	-7.2±0.67	8.1±1.5	3.89±0.21	1.88±0.51	0.35±0.11	7.0±0.33	0.42±0.02	0.9±0.05	55.84±3.61	2,3
NGC 6121	-12.5±0.36	-19.93±0.49	70.7±0.2	6.34±0.06	0.24±0.08	0.93±0.02	6.46±1.26	0.11±0.04	0.97±0.01	50.01±2.46	2,3

Table 1. Summary of the orbital parameters obtained from the sampling of positions and velocities for the clusters in our sample. The reference for the PM measurement is given in the last column. Clusters in the noPM are marked with * after their name. The reference IDs are the following: (1) [Dinescu et al. \(1997\)](#); (2) [Dinescu et al. \(1999a\)](#); (3) [Dinescu et al. \(1999b\)](#); (4) [Dinescu et al. \(2003\)](#); (5) [Casetti-Dinescu et al. \(2007\)](#); (6) [Casetti-Dinescu et al. \(2010\)](#); (7) [Casetti-Dinescu et al. \(2013\)](#); (8) [Dambis \(2006\)](#); (9) [Küpper et al. \(2015\)](#); (10) [Rossi et al. \(2015\)](#); and (11) [Scholz et al. \(1996\)](#).

Name	μ_α	μ_δ	V_{los}	R_{apo}	R_{peri}	ecc	M_i	μ	ϕ	r_J	Refs
	mas/yr	mas/yr	km s ⁻¹	kpc	kpc		10 ⁵ M _⊙			pc	
NGC 6101	-1.77±1.49	-4.65±1.41	361.4±1.7	38.09±13.11	3.77±1.21	0.84±0.04	2.2±0.16	0.41±0.04	0.21±0.09	78.02±4.56	8
NGC 6144	-3.06±0.64	-5.11±0.72	193.8±0.6	3.23±0.16	1.77±0.09	0.29±0.04	2.75±0.09	0.21±0.02	0.64±0.02	26.68±1.37	2,3
NGC 6139	-3.65±0.38	-8.34±0.36	6.7±6.0	4.28±0.4	2.24±0.43	0.33±0.04	7.65±0.36	0.45±0.02	0.61±0.12	56.95±3.9	8
Terzan 3	-2.95±1.41	-6.35±1.35	-136.3±0.7	3.0±0.22	2.1±0.16	0.18±0.06	1.41±0.04	0.05±0.02	0.52±0.1	12.8±1.66	8
NGC 6171	-0.7±0.9	-3.1±1.0	-34.1±0.3	3.6±0.09	2.26±0.32	0.23±0.07	3.01±0.18	0.3±0.02	0.96±0.03	36.49±0.76	3
NGC 6205	-0.9±0.71	5.5±1.12	-244.2±0.2	25.39±5.23	5.65±0.31	0.64±0.06	8.6±0.53	0.52±0.01	0.15±0.04	113.26±3.51	3
NGC 6229*	–	–	–	34.43±4.26	11.81±6.09	0.51±0.18	5.5±0.37	0.52±0.01	0.78±0.19	222.63±10.08	–
NGC 6218	1.3±0.58	-7.83±0.62	-41.4±0.2	5.39±0.12	2.47±0.24	0.37±0.04	3.33±0.2	0.34±0.01	0.81±0.04	48.74±0.82	3
NGC 6235*	–	–	–	5.02±0.91	1.89±0.7	0.46±0.12	1.89±0.27	0.18±0.04	0.66±0.24	28.76±2.67	–
NGC 6254	-6.0±1.0	-3.3±1.0	75.2±0.7	5.02±0.1	3.13±0.33	0.23±0.05	3.64±0.22	0.39±0.01	0.91±0.01	52.97±0.69	3
NGC 6256*	–	–	–	3.5±0.58	1.1±0.45	0.54±0.14	3.52±0.37	0.23±0.04	0.75±0.18	30.76±3.03	–
Pal 15*	–	–	–	46.05±7.23	17.87±7.89	0.46±0.15	0.56±0.04	0.45±0.03	0.68±0.26	115.61±6.11	–
NGC 6266	-3.5±0.37	-0.82±0.37	-70.1±1.4	2.24±0.17	1.77±0.14	0.12±0.02	15.83±1.02	0.48±0.01	0.47±0.11	51.14±1.47	4
NGC 6273	-2.86±0.49	-0.45±0.51	135.0±4.1	2.85±0.2	0.72±0.21	0.59±0.09	15.65±0.46	0.44±0.02	0.41±0.04	42.2±2.99	6
NGC 6284	-3.66±0.64	-5.39±0.83	27.5±1.7	8.23±1.23	5.97±1.08	0.21±0.06	5.1±0.27	0.48±0.01	0.56±0.36	82.39±5.57	6
NGC 6287	-3.68±0.88	-3.54±0.69	-288.7±3.5	5.3±0.37	0.24±0.07	0.91±0.02	7.04±1.3	0.12±0.04	0.37±0.02	25.46±2.83	6
NGC 6293	0.26±0.85	-5.14±0.71	-146.2±1.7	3.28±0.35	0.31±0.09	0.82±0.04	7.34±0.84	0.19±0.04	0.53±0.06	27.99±3.45	6
NGC 6304	-2.59±0.29	-1.56±0.29	-107.3±3.6	3.09±0.18	1.9±0.1	0.24±0.01	3.41±0.2	0.31±0.01	0.56±0.04	31.43±0.68	4
NGC 6316	-2.42±0.63	-1.71±0.56	71.4±8.9	2.59±0.39	1.13±0.22	0.38±0.1	8.09±0.41	0.39±0.02	0.83±0.05	42.58±4.85	4
NGC 6341	-3.3±0.55	-0.33±0.7	-120.0±0.1	10.58±0.29	0.82±0.25	0.86±0.04	7.46±0.53	0.36±0.03	0.92±0.02	103.5±3.9	3
NGC 6325	-3.91±0.85	-5.4±0.74	29.8±1.8	1.24±0.04	0.24±0.05	0.68±0.06	7.32±1.12	0.08±0.02	0.99±0.01	15.66±1.41	8
NGC 6333	-0.57±0.57	-3.7±0.5	229.1±7.0	4.76±0.23	1.04±0.08	0.64±0.02	5.9±0.36	0.35±0.01	0.2±0.02	30.82±0.47	6
NGC 6342	-2.77±0.71	-5.84±0.65	115.7±1.4	2.0±0.08	0.93±0.04	0.36±0.02	2.92±0.03	0.11±0.02	0.68±0.03	15.95±1.24	6
NGC 6356	-3.14±0.68	-3.65±0.53	27.0±4.3	7.56±0.46	2.18±0.8	0.55±0.12	8.65±0.4	0.47±0.02	0.92±0.02	96.26±6.21	6
NGC 6355*	–	–	–	2.12±0.62	0.57±0.19	0.55±0.12	7.33±0.4	0.29±0.04	0.47±0.22	25.03±3.69	–
NGC 6352*	–	–	–	4.14±0.44	1.31±0.57	0.52±0.16	2.22±0.36	0.18±0.04	0.79±0.15	28.4±0.9	–
IC 1257	-4.81±0.64	-3.44±0.64	-140.2±2.1	1791.9±426.29	17.51±0.76	0.98±0.01	0.98±0.06	0.49±0.01	0.0±0.01	87.81±4.46	8
Terzan 2	-0.94±0.3	0.15±0.42	109.0±15.0	2.59±0.24	0.45±0.15	0.7±0.07	3.68±0.9	0.05±0.02	0.26±0.02	9.6±1.46	10
NGC 6366	-3.9±0.57	-6.13±0.52	-122.2±0.5	5.69±0.11	1.15±0.12	0.66±0.02	1.81±0.12	0.09±0.01	0.92±0.01	27.73±1.41	8
Terzan 4	3.5±0.69	0.35±0.58	-50.0±2.9	4.17±0.4	1.17±0.21	0.56±0.06	1.71±0.21	0.03±0.02	0.03±0.01	7.53±1.35	10
NGC 6362	-3.09±0.46	-3.83±0.46	-13.1±0.6	5.51±0.11	2.22±0.09	0.43±0.02	2.61±0.12	0.28±0.01	0.92±0.03	44.76±1.5	1,3
Liller 1	-4.6±0.83	-4.12±0.79	52.0±15.0	0.9±0.07	0.17±0.04	0.69±0.07	10.24±1.84	0.07±0.03	0.88±0.05	12.86±1.43	8
NGC 6380*	–	–	–	3.82±0.62	1.17±0.5	0.53±0.15	4.3±0.37	0.29±0.05	0.76±0.18	37.52±3.77	–
Terzan 1	0.51±0.31	-0.93±0.29	114.0±14.0	3.13±0.24	1.09±0.15	0.48±0.04	1.88±0.18	0.03±0.02	0.27±0.02	8.91±1.67	10
Ton 2	-2.97±0.81	-3.89±1.02	-184.4±2.2	2.28±0.14	1.28±0.09	0.28±0.05	2.4±0.09	0.11±0.02	0.16±0.06	13.41±0.89	8
NGC 6388	-1.9±0.45	-3.83±0.51	80.1±0.8	3.11±0.15	0.72±0.08	0.62±0.03	19.67±1.04	0.47±0.01	0.93±0.03	70.95±4.64	6
NGC 6402	-0.13±0.51	-5.42±0.51	-66.1±1.8	4.26±0.17	1.14±0.22	0.58±0.05	14.85±0.88	0.47±0.01	0.93±0.03	79.77±3.85	8
NGC 6401*	–	–	–	3.11±0.56	0.99±0.4	0.51±0.14	5.9±0.41	0.33±0.04	0.7±0.21	37.14±4.39	–
NGC 6397	3.69±0.29	-14.88±0.26	18.8±0.1	6.43±0.05	3.12±0.1	0.35±0.01	1.97±0.1	0.28±0.01	0.95±0.01	45.96±0.88	3,7
Pal 6	2.95±0.41	1.24±0.19	181.0±2.8	8.45±0.46	2.16±0.13	0.59±0.01	2.26±0.14	0.29±0.01	0.06±0.01	26.16±0.76	10
NGC 6426	-4.05±1.47	-6.63±0.65	-162.0±23.0	1819.11±415.72	13.3±0.65	0.99±0.01	1.55±0.1	0.5±0.01	0.0±0.01	88.74±4.72	8
Djorg 1	3.14±1.53	-6.76±0.68	-362.4±3.6	208.24±86.31	3.7±0.38	0.97±0.01	2.18±0.11	0.42±0.02	0.01±0.01	49.07±4.05	8
Terzan 5	-4.05±0.87	-2.65±0.78	-93.0±2.0	1.91±0.19	0.49±0.11	0.59±0.05	5.29±0.57	0.18±0.02	0.74±0.05	21.49±1.64	8
NGC 6440*	–	–	–	1.94±0.4	0.57±0.23	0.57±0.12	12.03±0.84	0.38±0.04	0.53±0.21	32.02±1.6	–
NGC 6441	-2.86±0.45	-3.45±0.76	16.5±1.0	3.66±0.36	0.6±0.08	0.71±0.05	23.99±1.47	0.48±0.01	0.98±0.02	86.88±7.88	6

Table 1 – continued

Name	μ_α	μ_δ	V_{los}	R_{apo}	R_{peri}	ecc	M_i	μ	ϕ	r_J	Refs
	mas/yr	mas/yr	km s ⁻¹	kpc	kpc		10 ⁵ M _⊙			pc	
Terzan 6*	–	–	–	2.13±0.43	0.74±0.28	0.48±0.15	5.2±0.6	0.24±0.04	0.57±0.26	23.38±1.8	–
NGC 6453	-1.09±0.78	-2.14±0.84	-83.7±8.3	4.05±0.41	1.11±0.26	0.56±0.07	3.62±0.2	0.25±0.04	0.78±0.05	35.88±3.95	8
UKS 1	-3.48±1.57	-4.34±1.2	57.0±6.0	1.0±0.11	0.48±0.11	0.32±0.1	5.04±0.64	0.11±0.02	0.86±0.08	12.31±1.06	8
NGC 6496	-2.39±1.0	-6.64±1.02	-112.7±5.7	4.76±0.52	2.97±0.53	0.24±0.05	2.88±0.13	0.37±0.03	0.57±0.17	41.48±3.45	8
Terzan 9	0.0±0.38	-3.07±0.49	59.0±10.0	1.54±0.18	1.23±0.15	0.11±0.03	2.08±0.2	0.03±0.02	0.23±0.15	7.25±1.66	10
Djorg 2	0.99±1.15	-1.9±1.41	99.0±99.0	2.65±0.46	0.91±0.35	0.49±0.14	3.58±0.48	0.19±0.04	0.67±0.21	22.87±1.26	8
NGC 6517	-4.86±0.93	-4.99±0.86	-39.6±8.0	4.17±0.26	1.47±0.38	0.47±0.08	7.17±0.34	0.41±0.03	0.94±0.04	59.14±4.28	8
Terzan 10	1.88±0.19	-3.41±0.22	99.0±99.0	3.13±0.45	1.06±0.44	0.5±0.15	2.57±0.45	0.13±0.03	0.73±0.19	20.99±1.24	10
NGC 6522	6.08±0.2	-1.83±0.2	-21.1±3.4	4.3±0.18	0.66±0.2	0.73±0.06	5.17±0.57	0.26±0.03	0.05±0.01	16.19±1.82	4
NGC 6535	3.3±0.83	-6.85±0.83	-215.1±0.5	4.86±0.22	2.97±0.48	0.25±0.07	1.03±0.11	0.06±0.01	0.56±0.15	16.84±1.08	8
NGC 6528	-0.35±0.23	0.27±0.26	206.6±1.4	3.79±0.19	0.55±0.03	0.73±0.02	3.6±0.13	0.11±0.02	0.06±0.02	9.7±0.98	4
NGC 6539	-6.24±0.55	-1.23±0.64	31.0±1.7	4.24±0.28	1.47±0.13	0.48±0.05	7.43±0.45	0.41±0.01	0.6±0.06	50.76±1.29	8
NGC 6540	0.07±0.4	1.9±0.57	-17.7±1.4	4.9±0.32	2.97±0.17	0.24±0.03	1.69±0.1	0.23±0.02	0.03±0.01	25.22±0.64	10
NGC 6544*	–	–	–	5.88±0.45	1.78±0.71	0.54±0.14	2.69±0.3	0.27±0.05	0.85±0.12	45.13±1.51	–
NGC 6541*	–	–	–	2.92±0.49	0.96±0.42	0.53±0.15	9.62±0.69	0.39±0.03	0.67±0.22	43.9±0.7	–
NGC 6553	2.5±0.07	5.35±0.08	-3.2±1.5	11.09±0.2	2.33±0.18	0.65±0.02	4.56±0.27	0.42±0.01	0.01±0.01	36.93±0.99	4
NGC 6558	-0.12±0.55	0.47±0.6	-197.2±1.5	4.25±0.33	1.05±0.09	0.61±0.02	2.54±0.15	0.14±0.02	0.05±0.02	13.17±0.97	10
IC 1276	-17.13±0.6	-13.4±0.67	155.7±1.3	28.03±4.72	0.72±0.17	0.95±0.01	3.06±0.32	0.15±0.03	0.12±0.03	31.37±1.47	8
Terzan 12*	–	–	–	4.23±0.47	1.41±0.58	0.5±0.15	1.5±0.41	0.03±0.02	0.77±0.18	13.79±2.53	–
NGC 6569*	–	–	–	3.55±0.63	1.07±0.5	0.53±0.17	7.76±0.51	0.39±0.04	0.7±0.2	46.88±5.19	–
NGC 6584	-0.22±0.62	-5.79±0.67	222.9±15.0	12.86±1.69	1.19±0.44	0.83±0.04	4.74±0.24	0.35±0.05	0.48±0.07	69.47±5.53	1,3
NGC 6624*	–	–	–	1.95±0.49	0.5±0.12	0.61±0.1	5.32±0.55	0.21±0.03	0.52±0.2	19.66±0.62	–
NGC 6626	0.63±0.67	-8.46±0.67	17.0±1.0	3.17±0.18	0.78±0.15	0.6±0.06	7.21±0.5	0.34±0.02	0.95±0.04	46.4±0.85	3,7
NGC 6638	-0.56±1.48	-4.06±1.38	18.1±3.9	2.52±0.42	0.32±0.1	0.76±0.07	5.72±1.08	0.12±0.04	0.79±0.09	22.6±2.9	8
NGC 6637	-3.51±1.29	-2.4±1.2	39.9±2.8	2.05±0.24	0.67±0.12	0.49±0.07	5.19±0.17	0.26±0.03	0.71±0.12	24.93±2.14	8
NGC 6642	0.52±1.08	-3.72±1.2	-57.2±5.4	2.49±0.19	0.25±0.06	0.81±0.04	6.13±1.06	0.07±0.02	0.66±0.06	17.44±1.93	8
NGC 6652	4.75±0.07	-4.45±0.1	-111.7±5.8	8.1±0.7	2.17±0.23	0.58±0.01	2.1±0.01	0.28±0.02	0.08±0.02	26.3±1.91	10
NGC 6656	7.37±0.5	-3.95±0.42	-146.3±0.2	9.14±0.24	2.92±0.09	0.51±0.01	8.48±0.55	0.48±0.01	0.37±0.02	78.98±0.85	3,7
Pal 8*	–	–	–	6.22±0.86	1.97±0.92	0.52±0.17	1.36±0.37	0.11±0.04	0.78±0.17	25.92±2.62	–
NGC 6681	2.68±0.81	-3.78±0.91	220.3±0.9	6.77±0.94	0.39±0.08	0.89±0.03	5.16±0.62	0.13±0.02	0.25±0.03	22.22±1.56	8
NGC 6712	4.2±0.4	-2.0±0.4	-107.6±0.5	6.4±0.27	0.83±0.06	0.77±0.02	4.49±0.24	0.27±0.02	0.51±0.03	41.35±1.13	3
NGC 6715	-1.75±0.43	-4.95±0.6	141.3±0.3	160.26±52.92	15.64±0.76	0.82±0.05	29.87±1.73	0.55±0.01	0.02±0.01	287.11±13.8	8
NGC 6717*	–	–	–	3.25±0.52	1.16±0.46	0.5±0.13	2.18±0.43	0.07±0.02	0.65±0.21	16.3±1.0	–
NGC 6723	-0.17±0.45	-2.16±0.5	-94.5±3.6	3.35±0.21	1.36±0.08	0.41±0.04	5.37±0.23	0.34±0.01	0.6±0.06	37.4±1.88	4
NGC 6749	1.85±0.97	-7.1±1.5	-61.7±2.9	5.44±0.17	2.0±0.48	0.46±0.09	2.25±0.14	0.25±0.04	0.88±0.06	39.69±1.96	8
NGC 6752	-0.69±0.42	-2.85±0.45	-26.7±0.2	5.73±0.1	4.39±0.16	0.13±0.01	4.34±0.27	0.44±0.01	0.82±0.06	63.14±0.97	1,3
NGC 6760	0.46±0.67	-5.0±0.58	-27.5±6.3	5.28±0.13	1.74±0.1	0.51±0.03	5.08±0.27	0.38±0.01	0.91±0.03	59.58±1.72	8
NGC 6779	0.3±1.0	1.4±1.0	-135.6±0.9	14.11±1.1	0.83±0.24	0.89±0.02	4.34±0.31	0.25±0.04	0.64±0.06	74.85±3.92	3
Terzan 7*	–	–	–	19.14±3.2	8.39±2.7	0.42±0.12	0.44±0.04	0.29±0.05	0.62±0.28	50.3±3.6	–
Pal 10*	–	–	–	7.31±0.54	2.26±0.94	0.54±0.15	1.34±0.28	0.16±0.05	0.85±0.11	34.33±2.04	–
Arp 2	-0.04±1.22	-2.82±1.25	115.0±10.0	44.85±11.69	12.74±2.93	0.61±0.05	0.48±0.03	0.41±0.03	0.25±0.16	71.91±4.09	–
NGC 6809	-1.42±0.62	-10.25±0.64	174.7±0.3	5.76±0.13	1.38±0.18	0.61±0.05	4.47±0.24	0.31±0.02	0.62±0.01	46.5±0.7	2,3
Terzan 8*	–	–	–	24.12±4.09	10.67±3.55	0.41±0.12	0.43±0.04	0.33±0.05	0.58±0.28	60.69±4.08	8
Pal 11	-2.36±1.16	0.19±0.96	-68.0±10.0	13.08±2.8	5.92±1.28	0.43±0.08	2.09±0.12	0.43±0.03	0.29±0.2	63.46±3.75	8
NGC 6838	-2.3±0.8	-5.1±0.8	-22.8±0.2	6.99±0.02	4.49±0.04	0.22±0.01	0.87±0.04	0.22±0.01	0.99±0.01	34.71±0.98	3

Table 1 – continued

Name	μ_α	μ_δ	V_{los}	R_{apo}	R_{peri}	ecc	M_i	μ	ϕ	r_J	Refs
	mas/yr	mas/yr	km s ⁻¹	kpc	kpc		10 ⁵ M _⊙			pc	
NGC 6864	-0.64±1.56	-3.34±1.31	-189.3±3.6	19.23±2.79	6.8±2.93	0.54±0.12	8.77±0.59	0.52±0.01	0.62±0.21	160.94±8.79	8
NGC 6934	1.2±1.0	-5.1±1.0	-411.4±1.6	45.32±13.86	7.01±1.59	0.76±0.06	3.18±0.17	0.49±0.01	0.14±0.07	103.08±4.49	8
NGC 6981	-1.62±1.68	-11.28±1.33	-345.0±3.7	1841.6±243.73	10.66±0.46	0.99±0.01	2.12±0.09	0.5±0.01	0.0±0.01	90.82±2.96	8
NGC 7006	-0.96±0.35	-1.14±0.4	-384.1±0.4	118.52±35.85	18.14±4.14	0.75±0.02	3.8±0.25	0.52±0.01	0.2±0.1	233.22±10.63	8
NGC 7078	-0.95±0.51	-5.63±0.5	-107.0±0.2	11.08±0.43	6.3±0.81	0.28±0.04	15.29±0.96	0.53±0.01	0.89±0.07	158.56±5.95	3
NGC 7089	5.9±0.86	-4.95±0.86	-5.3±2.0	41.84±10.67	5.84±0.82	0.76±0.05	13.16±0.78	0.53±0.01	0.12±0.05	149.59±5.55	3
NGC 7099	1.42±0.69	-7.71±0.65	-184.2±0.2	7.45±0.21	2.82±0.42	0.45±0.06	3.56±0.18	0.38±0.02	0.95±0.03	67.86±2.72	2
Pal 12	-1.2±0.3	-4.21±0.29	27.8±1.5	24.85±3.66	15.51±0.51	0.23±0.06	0.23±0.01	0.38±0.02	0.02±0.02	46.04±2.22	8
Pal 13	2.3±0.26	0.27±0.25	25.2±0.3	153.46±34.77	12.35±1.23	0.85±0.02	0.14±0.01	0.28±0.03	0.1±0.03	49.69±2.46	8
NGC 7492*	–	–	–	30.68±4.93	11.85±4.88	0.47±0.14	0.75±0.06	0.43±0.03	0.7±0.25	96.11±4.92	–

Table 1 – *continued*

REFERENCES

- Ahn C. P., et al., 2014, *ApJS*, **211**, 17
- Alexander P. E. R., Gieles M., 2012, EMACSS: Evolve Me A Cluster of StarS, Astrophysics Source Code Library (ascl:1203.006)
- Alexander P. E. R., Gieles M., Lamers H. J. G. L. M., Baumgardt H., 2014, *MNRAS*, **442**, 1265
- Amorisco N. C., 2015, *MNRAS*, **450**, 575
- Anders P., Lamers H. J. G. L. M., Baumgardt H., 2009, *A&A*, **502**, 817
- Balbinot E., Santiago B. X., da Costa L. N., Makler M., Maia M. A. G., 2011, *MNRAS*, **416**, 393
- Baumgardt H., 2001, *MNRAS*, **325**, 1323
- Baumgardt H., Makino J., 2003, *MNRAS*, **340**, 227
- Belokurov V., Evans N. W., Irwin M. J., Hewett P. C., Wilkinson M. I., 2006, *ApJ*, **637**, L29
- Bernard E. J., et al., 2016, *MNRAS*, **463**, 1759
- Bonaca A., Geha M., Küpper A. H. W., Diemand J., Johnston K. V., Hogg D. W., 2014, *ApJ*, **795**, 94
- Bovy J., 2015, *ApJS*, **216**, 29
- Bressan A., Marigo P., Girardi L., Salasnich B., Dal Cero C., Rubele S., Nanni A., 2012, *MNRAS*, **427**, 127
- Bruzual G., Charlot S., 2003, *MNRAS*, **344**, 1000
- Cai M. X., Gieles M., Heggie D. C., Varri A. L., 2016, *MNRAS*, **455**, 596
- Casetti-Dinescu D. I., Girard T. M., Herrera D., van Altena W. F., López C. E., Castillo D. J., 2007, *AJ*, **134**, 195
- Casetti-Dinescu D. I., Girard T. M., Korchagin V. I., van Altena W. F., López C. E., 2010, *AJ*, **140**, 1282
- Casetti-Dinescu D. I., Girard T. M., Jílková L., van Altena W. F., Podestá F., López C. E., 2013, *AJ*, **146**, 33
- Claydon I., Gieles M., Zocchi A., 2016, *MNRAS*, **455**, 596
- Conroy C., Gunn J. E., 2010, *ApJ*, **712**, 833
- Contenta F., Gieles M., Balbinot E., Collins M. L. M., 2017, *MNRAS*, **466**, 1741
- Dambis A. K., 2006, *Astronomical and Astrophysical Transactions*, **25**, 185
- Dinescu D. I., Girard T. M., van Altena W. F., Mendez R. A., Lopez C. E., 1997, *AJ*, **114**, 1014
- Dinescu D. I., van Altena W. F., Girard T. M., López C. E., 1999a, *AJ*, **117**, 277
- Dinescu D. I., Girard T. M., van Altena W. F., 1999b, *AJ*, **117**, 1792
- Dinescu D. I., Girard T. M., van Altena W. F., López C. E., 2003, *AJ*, **125**, 1373
- Dormand J., Prince P., 1980, *Journal of Computational and Applied Mathematics*, **6**, 19
- Erkal D., Belokurov V., Bovy J., Sanders J. L., 2016, *MNRAS*, **463**, 102
- Eyre A., Binney J., 2009, *MNRAS*, **400**, 548
- Fardal M. A., Huang S., Weinberg M. D., 2015, *MNRAS*, **452**, 301
- Forbes D. A., Bridges T., 2010, *MNRAS*, **404**, 1203
- Fukushige T., Heggie D. C., 2000, *MNRAS*, **318**, 753
- Gibbons S. L. J., Belokurov V., Evans N. W., 2014, *MNRAS*, **445**, 3788
- Gieles M., Heggie D. C., Zhao H., 2011, *MNRAS*, **413**, 2509
- Gieles M., Alexander P. E. R., Lamers H. J. G. L. M., Baumgardt H., 2014, *MNRAS*, **437**, 916
- Grillmair C. J., Dionatos O., 2006, *ApJ*, **641**, L37
- Grillmair C. J., Johnson R., 2006, *ApJ*, **639**, L17
- Grillmair C. J., Jarrett T. H., Ha A. C., 2004, in Prada F., Martinez Delgado D., Mahoney T. J., eds, *Astronomical Society of the Pacific Conference Series Vol. 327, Satellites and Tidal Streams*. p. 276
- Halford M., Zaritsky D., 2015, *ApJ*, **815**, 86
- Harris W. E., 1976, *AJ*, **81**, 1095
- Harris W. E., 1996, *AJ*, **112**, 1487
- Harris W. E., 2010, preprint, (1012.3224:1012.3224)
- Helmi A., White S. D. M., 1999, *MNRAS*, **307**, 495
- Hénon M., 1961, *Annales d'Astrophysique*, **24**, 369; English translation: [ArXiv:1103.3499](https://arxiv.org/abs/1103.3499)
- Hurley J. R., Pols O. R., Tout C. A., 2000, *MNRAS*, **315**, 543
- King I., 1962, *AJ*, **67**, 471
- Koch A., Grebel E. K., Odenkirchen M., Martínez-Delgado D., Caldwell J. A. R., 2004, *AJ*, **128**, 2274
- Koposov S. E., Rix H.-W., Hogg D. W., 2010, *ApJ*, **712**, 260
- Kroupa P., 2001, *MNRAS*, **322**, 231
- Kruijssen J. M. D., 2009, *A&A*, **507**, 1409
- Küpper A. H. W., Lane R. R., Heggie D. C., 2012, *MNRAS*, **420**, 2700
- Küpper A. H. W., Balbinot E., Bonaca A., Johnston K. V., Hogg D. W., Kroupa P., Santiago B. X., 2015, *ApJ*, **803**, 80
- Küpper A. H. W., Johnston K. V., Mieske S., Collins M. L. M., Tollerud E. J., 2017, *ApJ*, **834**, 112
- Kuzma P. B., Da Costa G. S., Mackey A. D., Roderick T. A., 2016, *MNRAS*, **461**, 3639
- LSST Dark Energy Science Collaboration 2012, preprint, ([arXiv:1211.0310](https://arxiv.org/abs/1211.0310))
- Lamers H. J. G. L. M., Baumgardt H., Gieles M., 2013, *MNRAS*, **433**, 1378
- Lane R. R., Küpper A. H. W., Heggie D. C., 2012, *MNRAS*, **423**, 2845
- Lee K. H., Lee H. M., Fahlman G. G., Lee M. G., 2003, *AJ*, **126**, 815
- Leon S., Meylan G., Combes F., 2000, *A&A*, **359**, 907
- Miyamoto M., Nagai R., 1975, *PASJ*, **27**, 533
- Moore B., 1996, *ApJ*, **461**, L13
- Moreno E., Pichardo B., Velázquez H., 2014, *ApJ*, **793**, 110
- Myeong G. C., Jerjen H., Mackey D., Da Costa G. S., 2017, *ApJ*, **840**, L25
- Navarrete C., Belokurov V., Koposov S. E., 2017, *ApJ*, **841**, L23
- Navarro J. F., Frenk C. S., White S. D. M., 1996, *ApJ*, **462**, 563
- Newberg H. J., et al., 2002, *ApJ*, **569**, 245
- Niederste-Ostholt M., Belokurov V., Evans N. W., Gilmore G., Wyse R. F. G., Norris J. E., 2009, *MNRAS*, **398**, 1771
- Niederste-Ostholt M., Belokurov V., Evans N. W., Koposov S., Gieles M., Irwin M. J., 2010, *MNRAS*, **408**, L66
- Odenkirchen M., et al., 2001, *ApJ*, **548**, L165
- Odenkirchen M., Grebel E. K., Dehnen W., Rix H.-W., Cudworth K. M., 2002, *AJ*, **124**, 1497
- Paust N. E. Q., et al., 2010, *AJ*, **139**, 476
- Pearson S., Küpper A. H. W., Johnston K. V., Price-Whelan A. M., 2015, *ApJ*, **799**, 28
- Peebles P. J. E., 1984, *ApJ*, **277**, 470
- Price-Whelan A. M., Johnston K. V., Valluri M., Pearson S., Küpper A. H. W., Hogg D. W., 2016, *MNRAS*, **455**, 1079
- Renaud F., Gieles M., 2015, *MNRAS*, **449**, 2734
- Renaud F., Agertz O., Gieles M., 2017, *MNRAS*, **465**, 3622
- Rossi L. J., Ortolani S., Barbuy B., Bica E., Bonfanti A., 2015, *MNRAS*, **450**, 3270
- Scholz R.-D., Odenkirchen M., Hirte S., Irwin M. J., Borngen F., Ziener R., 1996, *MNRAS*, **278**, 251
- Schönrich R., Binney J., Dehnen W., 2010, *MNRAS*, **403**, 1829
- Sesar B., et al., 2015, *ApJ*, **809**, 59
- Sollima A., Dalessandro E., Beccari G., Pallaanca C., 2017, *MNRAS*, **464**, 3871
- The Dark Energy Survey Collaboration 2005, *ArXiv Astrophysics e-prints*, Thomas G. F., Ibata R., Famaey B., Martin N. F., Lewis G. F., 2016, *MNRAS*, **460**, 2711
- VandenBerg D. A., Brogaard K., Leaman R., Casagrande L., 2013, *ApJ*, **775**, 134
- Webb J. J., Vesperini E., Dalessandro E., Beccari G., Ferraro F. R., Lanzoni B., 2017, preprint, ([arXiv:1707.06653](https://arxiv.org/abs/1707.06653))
- Willman B., et al., 2006, *ArXiv Astrophysics e-prints*, van den Bosch F. C., Lewis G. F., Lake G., Stadel J., 1999, *ApJ*, **515**, 50